Flow fields around active droplets squeezing through tight confinements

Subhasish Guchhait [1,*] Smita S. Sontakke [1,*] Shubhadeep Mandal [2] and Ranabir Dey [1,†]

[1]*Department of Mechanical and Aerospace Engineering, Indian Institute of Technology Hyderabad, Kandi, Sangareddy, Telangana 502285, India*

[2]*Department of Mechanical Engineering, Indian Institute of Science, Bengaluru 560012, India*

(Received 9 July 2024; accepted 28 February 2025; published 8 April 2025)

Biological microswimmers, like euglena, deform their body shape to swim through tight confinements having length scales comparable to the microswimmer length scale. Recently, it was shown that self-propelling active droplets can also squeeze through tight microconfinements by elongating their shape. However, the evolution of the velocity field generated by the active droplet as it deforms its shape to swim through increasingly tight microconfinements has remained scarcely studied. Using high-resolution fluorescence microscopy and μ-particle image velocimetry analysis, we show here that as the swimming active droplet deforms from a spherical shape to a "stadiumlike" shape, and eventually to an elongated "capsulelike" shape in increasingly tighter microchannels, its hydrodynamic signature gradually changes from a symmetric, quadrupolar velocity field to an asymmetric velocity field. We characterize such alterations in the active droplet dynamics using the distributions of the local velocity magnitude, axial and transverse components of the local flow velocity, vorticity, and the ejected filled micelle concentration. Finally, we use finite-element-method-based numerical simulations to provide a qualitative understanding of the evolution of the velocity field stemming from the underlying physicochemical hydrodynamics in presence of a thin lubrication film. The present work delineates the chemohydrodynamic characteristics of active droplets navigating extreme confined spaces, which can be beneficial for many autonomous cargo-delivery applications in complex environment.

DOI: 10.1103/PhysRevFluids.10.044202

I. INTRODUCTION

Motile microorganisms like algae, bacteria, and protozoa, e.g., *paramecium*, are typically found in diverse environments, such as in natural water bodies [1,2], in soil [3,4], and even within the human body [5,6]. For their survival in complex environment, these biological microswimmers need to navigate through confined spaces, like in soil [3,4,7] and through mucus network [8–10], and adopt various swimming strategies for efficient uptake of oxygen and nutrients. To understand these survival strategies of biological microswimmers, it is then important to understand how confined spaces alter the swimming dynamics of microswimmers.

Some studies on *Escherichia coli* in microchannels indicate that these bacteria tend to swim near corners and walls in wider channels [11,12]. Their swimming velocity increases, reaching a peak value as the channel cross-section decreases, and they eventually switch to swimming along the axis of the channel [11]. In even tighter confinements, swimming velocity of *E. coli* decreases, and they navigate through the channel by growing and dividing their cells [13]. *Euglena* [14] and

*These authors contributed equally to this work.
†Contact author: ranabir@mae.iith.ac.in

paramecium [15,16] can also swim through a tight confinement by deforming their body shape and by adopting a cylindrical shape, respectively. During such swimming in tight confinements, these microswimmers never come in direct contact with the walls of the confinement, which may be attributed to the existence of a thin lubricating film between the wall and the body of the microswimmer. The role of an intervening thin film in altering the swimming characteristics of microswimmers in tight confinements remains scarcely studied. Such studies can subsequently aid in designing applications in which self-propelling, artificial microswimmers need to navigate tight confinements, e.g., in targeted cargo delivery for biomedical applications [17,18].

Over the past decade or so, researchers have designed self-propelling artificial microswimmers which mimic the motility, and often the hydrodynamic signature, of biological microswimmers. These self-propelling artificial microswimmers can be of two types—first, there are the Janus particles [19–23] having an engineered material asymmetry. Janus colloidal particles self-propel due to phoretic effects [24,25] stemming from catalytic reactions, such as self-diffusiophoresis [26], self-electrophoresis [27], or self-thermophoresis [28,29]. Second, there are the isotropic active oil/water droplets [30–39] which self-propel in surfactant solutions by generating a surface tension gradient along the interface due to spontaneous symmetry breaking of the interfacial surfactant monomer concentration. From the perspective of applications, active droplets have certain advantages over active catalytic colloids—(i) the former being essentially isotropic microscale oil/water droplets can be generated on-demand using standard microfluidic techniques by circumventing involved fabrication methodologies necessary for engineering Janus colloids; (ii) active droplets use ionic surfactant solutions as their fuel which can be chosen for their biocompatibility unlike the corrosive chemicals, like hydrogen peroxide, necessary as fuels for active colloids. Hence, it is logical to conclude that active droplets can be a more viable alternative as autonomous microcarriers for applications like targeted cargo delivery in biomedical settings. However, in applications like targeted cargo delivery, both active droplets and catalytic Janus colloids, more often than not, need to navigate narrow confinements having length scales typically of the order of the swimmer length scale [40].

Over the years, substantial theoretical efforts have been made to understand the effects of microchannel/microcapillary geometry, cross-section, and size on the dynamics of self-propelled microswimmers in confinements [41–46]. On the experimental front, it was demonstrated that catalytic Janus colloids are attracted toward, and tend to swim along, solid boundaries [47]—a proclivity which can be exploited to guide these self-propelled microswimmers toward a desired target. Furthermore, catalytic Janus microswimmers also demonstrated a substantial increase in their swimming speed with increasing tightness of the confinement [48]. In case of active droplets, investigations were conducted to delineate their swimming characteristics near a confining wall [49], in complex microfluidic geometries [50,51], and even in the midst of micropillar arrays [51,52]. Fascinatingly, active droplets can "sense" surfactant concentration gradients enabling them to swim through complex microfluidic networks in a manner reminiscent of autochemotactic swimming strategies [50,51]. Near a micropillar, active droplets exhibit an attraction toward, or repulsion away from, a pillar depending on the radius of curvature [52]. Recently, efforts were also made to delineate the emergent interfacial hydrodynamics of immobilized active droplets behaving as micropumps [53], and to understand how the underlying physicochemical hydrodynamics shapes mutual interactions among active droplets in confinements [54]. At this point, it is interesting to wonder whether active droplets can autonomously squeeze through tight microchannels having length scales smaller than the microswimmer length scale by deforming their shape, in a manner analogous to biological microswimmers, like *euglena* [14] and *paramecium* [15,16].

In an interesting recent work [55], it was demonstrated that active water droplets can indeed squeeze through tight microchannels, straight or converging-diverging, by elongating their shape. With increasing confinement, the elongated active droplets undergo spontaneous division at their posterior end [55]. The aforementioned behavior of active droplets was explained by considering the chemohydrodynamics in presence of a surrounding lubricating thin film, in a manner similar to the classical Bretherton approach [55]. In a subsequent theoretical work [56], the self-propulsion of

an isotropic, autophoretic spherical particle in a tight capillary was also explained, with a special emphasis on the physicochemical hydrodynamics considering the thin lubrication layer. Except for a brief effort in Ref. [55], the evolution of the hydrodynamic signature (flow field) of an active droplet as it spontaneously adapts its shape to swim through increasingly tighter confinement has remained unstudied. Such an investigation will provide a clear understanding of how the coupling of the shape (geometry) of the microswimmer and the underlying physicochemical hydrodynamics, in the presence of a thin lubricating film, alters the velocity field and chemical distribution as the active droplet autonomously squeezes through a tight confinement.

In this work, we physcially explain the evolution in the velocity field generated by increasingly larger self-propelled oil droplets as they squeeze through a tight rectangular microchannel using high-resolution fluorescence microscopy and quantitative microparticle image velocimetry (μ-PIV) analysis. We show that as the active droplet becomes increasingly bigger relative to the tight microchannel, it adapts its shape from spherical to "stadiumlike", and finally to an elongated "capsulelike" shape to spontaneously squeeze through the microconfinement. Interestingly, during this shape evolution, the active droplet gradually alters its quadrupolar, symmetric hydrodynamic signature to an asymmetric velocity field characterized by two circulation zones at the anterior and posterior. To better understand the dynamics of the self-propelling active droplet, we also perform fluorescence microscopy analysis to delineate the ejected filled micelle concentration around the active droplet corresponding to the varying shapes in the tight microchannel. Finally, we complement our experimental observations with a full-scale numerical simulation of the coupled hydrodynamic and the surfactant advection-diffusion problem for the active droplet of different shapes in a tight microchannel. We provide a physical understanding of the evolution in swimming characteristics of active droplets with increasing confinement effect by correlating the experimentally observed velocity and filled micelle concentration fields, and the results of our detailed numerical simulation. Detailed knowledge of the evolution of the shape, velocity field and chemical concentrations related to active droplets with increasingly tighter microconfinements will be beneficial for better understanding their dynamics and swimming efficiency in a complex, constricted environment.

To explain the aforementioned techniques and results, this article is structured as follows: In Sec. II, we describe in detail the various experimental setups and methodologies; in Sec. III, we describe the details of the numerical simulation technique; in Sec. IV, we present and discuss the results obtained through the various experimental techniques; in Sec. V, we explain the experimental observations with the help of the numerical simulation results; and in Sec. VI, we summarize our findings and discuss their consequences for future endeavors.

II. EXPERIMENTAL SETUP AND METHODOLOGY

A. Fabrication of PDMS microchannels

We use the well-established photolithography and soft-lithography techniques to fabricate the microchannels used in this work. We pour polydimethylsiloxane (PDMS) mixture, consisting of Sylgard 184 prepolymer and crosslinker in the weight ratio of $10:1$, onto the silicon wafers containing microfluidic channel moulds fabricated using SU8 photoresist. Subsequently, we cure the PDMS at 75°C in a hot air oven for a duration of 3 h. Using this procedure, we fabricate two types of microfluidic chips: (i) a flow-focusing cross junction for generating active droplets, and (ii) microfluidic chips containing multiple channels connected to single inlet and outlet reservoirs (see Supplementary Material Fig. S1 [57]). Each microchannel has a height of $h = 50$ μm and a width of $w = 64$ μm [Fig. 1(a)]. Finally, the cured PDMS stamps are bonded to PDMS-coated coverslips (thickness: 160 μm) using plasma oxidation.

B. Generation of active droplets

We use slowly solubilizing CB15 oil [(S)-4-Cyano-4′-(2-methyl butyl) biphenyl; Tokyo Chemical Industry] droplets in a supramicellar aqueous solution of cationic surfactant

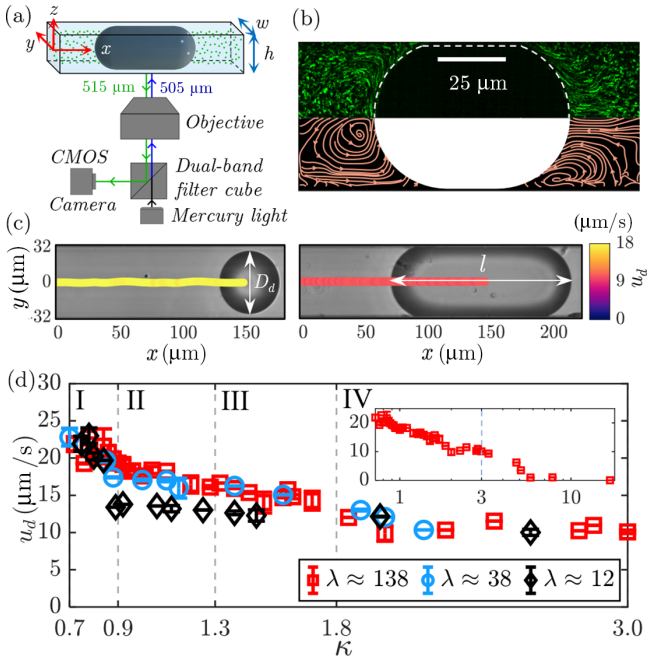

FIG. 1. (a) Schematic of an elongated active droplet inside a rectangular microchannel, with the microscopy setup. (b) A fluorescence micrograph depicting the flow around a self-propelling active droplet (for $\kappa = \frac{D_d}{D_h}$ or $\frac{l}{D_h} = 1.50$) (top half), and the corresponding streamline pattern obtained using μPIV analysis (bottom half). (c) Bright-field microscopy images showing the active droplet trajectory inside the microchannel color-coded with the swimming velocity u_d of the droplet for (left) spherical ($\kappa < 1.00$) and (right) elongated ($\kappa = 3$) droplets. (d) Variation of the steady-state droplet swimming speed with increasing confinement effect (κ), for different swimming medium viscosity μ_e (here $\lambda = \mu_i/\mu_e$, where $= \mu_i$ is the constant active droplet viscosity). The inset illustrates the same for κ till ∼17, in which case the active droplet ceases to move.

Tetradecyltrimethylammonium bromide, TTAB [critical micelle concentration (CMC) = 0.13 wt.%; Sigma-Aldrich] as the active droplet system [32,33,36,39]. First, we generate CB15 droplets in 0.1 wt% aqueous surfactant solution using the flow-focusing crossjunction chip (see Supplemental Material Fig. S1 [57]). We use four different sizes (diameter D_d) of the droplets for the experiments reported here—45.33 ± 3.01 μm; 55.72 ± 3.89 μm; 67.6 ± 2.86 μm; and 80.64 ± 6.39 μm. We make these droplets active, i.e., self-propelling, by mixing the 0.1 wt% aqueous surfactant solution (containing monodispersed droplets) in 7.5 wt% aqueous surfactant solution (surfactant concentration above CMC) in a 1 : 2 ratio.

These active droplets self-propel due to micellar solubilization [32,33,36,39]. During this solubilization process, empty micelles in the aqueous solution take up oil molecules and additional surfactant monomers from the interfacial region, and grow into filled micelles. Due to any advective perturbation, the initially isotropic distribution of filled and empty micelles around the droplet gets spontaneously broken, resulting in local enhancement (reduction) in filled to empty micelle ratio along the interfacial region. This locally reduces (enhances) the interfacial surfactant monomer coverage, setting up an interfacial tension variation inversely proportional to the local surfactant monomer coverage. Such spontaneously created interfacial tension gradient along the droplet interface in turn sets up a local Marangoni stress. This Marangoni stress triggers an interfacial velocity toward the region of lower surfactant coverage (away from the region of higher empty micelle concentration and toward the region of higher filled micelle concentration). To satisfy the noninertial constraints of the system, the oil droplet starts to self-propel in the direction of higher

concentration of empty micelles, thereby maintaining a self-sustaining interfacial tension gradient. As the active droplets swim in a quasi-ballistic manner, they leave behind a trail of filled micelles in their wake [62,63].

C. Bright-field microscopy

We use bright-field microscopy (with an inverted Nikon ECLIPSE Ti microscope) at 30× magnification to characterize the trajectories of the self-propelled active droplets of varying sizes in the microchannel with a fixed rectangular cross-section. The extent to which the active droplet is confined in the microchannel is characterized by the nondimensional parameter κ, where for spherical droplets $\kappa = D_d/D_h$, and for elongated droplets $\kappa = l/D_h$. Here, D_d is the diameter of spherical droplet, l is the maximum length of the elongated active droplet, and D_h is the hydraulic diameter of the channel defined as $4wh/(2(w+h)) = 56.14$ μm. Higher values of κ indicate a tighter confinement relative to the characteristic length scale of the droplet. For $\kappa < 1.30$, the active droplet swims in the microchannel with a spherical or nearly spherical shape [Fig. 1(c) left]. For $1.30 < \kappa \leqslant 1.80$, the swimming droplets adopt a "stadiumlike" shape [64] inside the microchannel [Fig. 1(b)]. Finally, the droplets exhibit an elongated shape, like a capsule [65], for $\kappa > 1.80$ as they swim in the microchannel [Fig. 1(c) right]. For $\kappa < 1.30$, the active droplets spontaneously enter the microchannel from the reservoir in which they are dispersed. However, for $\kappa > 1.30$, we "inject" the bigger active droplets into the microchannel using an imposed ambient flow. Subsequently, we wait till the ambient reaches a quiescent state before recording any image.

We record the videos at a frame capture rate of 25 fps (frame rate per second) using a CMOS monochrome digital camera (IDS Imaging) having 1920 × 1200 pixels in the $1/1.2''$ CMOS sensor. We determine the swimming trajectory, and calculate the instantaneous swimming velocity of the active droplet by tracking the centroid of the droplet projection in the microscopy image plane using an in-house image processing routine (in MATLAB R2020a) [Fig. 1(c)] (also see Supplemental Material Sec. II [57]). For the experiments reported herein, the droplets exhibit steady-state motion [Fig. 1(c)]. Hence, the measured instantaneous velocity of the droplets represents their steady swimming velocity. The minimum translation velocity that we can resolve using a 30× objective (with a spatial resolution of 0.176 μm/pixel) and a frame capture rate of 25 fps is 2.2 μm/s.

D. Fluorescence microscopy and microparticle image velocimetry (μPIV)

For varying κ, the velocity field generated by the active droplet during swimming in the microchannel is characterized using high-resolution fluorescence microscopy and subsequent microparticle image velocimetry (μPIV) analysis. The μPIV setup, consisting of the illumination modules and the dual-band filter cube (peak excitation and emission wavelengths: 487/562 nm and 523/630 nm), is integrated with the inverted Nikon ECLIPSE Ti microscope [Fig. 1(a)]. To visualize the flow field, we use 500 nm carboxylate-modified fluorescent microspheres (Thermo Fisher Scientific) having excitation/emission wavelengths of 505/515 nm. We carry out the subsequent analysis using the open-source PIVlab [66], and our in-house post-processing routine.

For the μPIV analysis using PIVlab, we use the Discrete Fourier transform (DFT) method to get the crosscorrelation matrix. We use multiple passes with 64 × 64 pixels interrogation area with a step size of 32 × 32 pixels, followed by a second pass of 32 × 32 pixels interrogation area with a step size of 16 × 16 pixels. We then extract the data sets containing the velocity vector field from PIVlab, and post-process these using an in-house MATLAB routine to generate the velocity contour plots and streamlines (Figs. 2 and 3), and the vorticity contour plots (Fig. 4) [see Appendix A 1 (Fig. 8) for details]. The average advective velocity around the droplet for $\kappa = 0.85$ [Fig. 2(a)] at a distance equal to the radius of the droplet ($\sim D_d/2$) from its circumference estimated from the μPIV analysis is 7.169 ± 0.3312 μm/s. In Fig. 1(b), a fluorescence micrograph depicting the flow field around an active droplet is shown in the top half, and the corresponding streamlines obtained from μPIV analysis are shown in the bottom half.

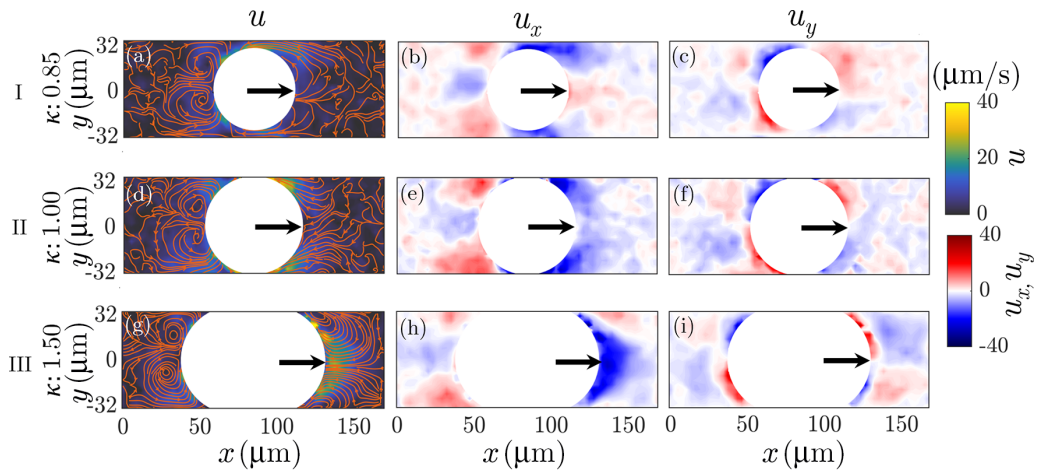

FIG. 2. Variations in the velocity field for swimming active droplets with increasing effect of the confinement (κ) as determined using fluorescence microscopy and μPIV analysis. (a)–(c) Regime-I ($\kappa \sim 0.85$), (d)–(f) Regime-II ($\kappa \sim 1.00$), and (g)–(i) Regime-III ($\kappa \sim 1.50$). In the left column, panels (a), (d), and (g) depict contour plots of the resultant local velocity (u), along with the streamlines. The middle column, panels (b), (e) and (h), and the right column, panels (c), (f) and (i), represent the distributions of the axial (u_x) and transverse (u_y) components of the local disturbance velocity, respectively. The black arrow denotes the direction of droplet motion.

E. Filled micelle trail visualization and kymographs

To visualize the filled micelle trail associated with the droplet microswimmer during its self-propulsion [62,63], we perform a separate set of experiments under identical conditions. In this case, we dye the CB15 oil with fluorescent Nile Red dye (Invitrogen^{TM}) (excitation/emission: 550/640 nm), and generate the oil droplets using similar droplet generation methodology. We then mix these Nile Red doped droplets in 7.5% aqueous TTAB solution to make them active, and introduce them in the microchannels. We use the identical inverted microscope setup with the dual

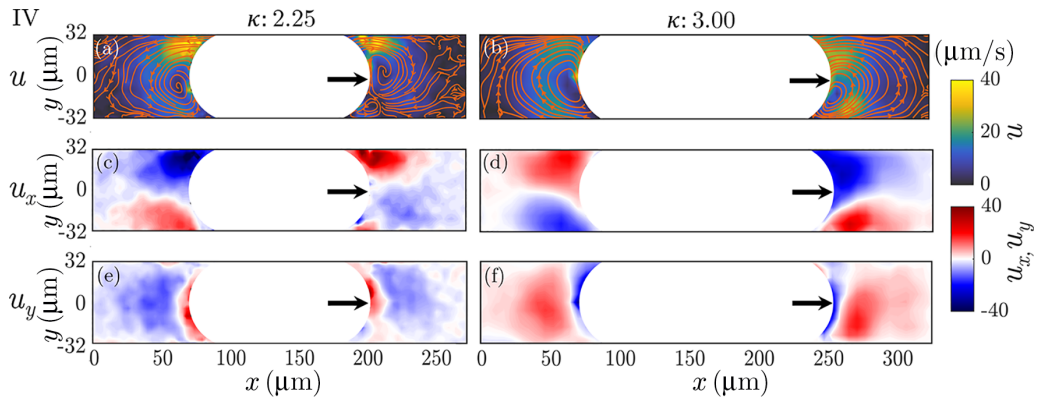

FIG. 3. Velocity fields for elongated ("capsulelike") active droplets for $\kappa > 1.80$ (Regime-IV) evaluated using fluorescence microscopy and μ-PIV analysis. The first row: (a) and (b), represents the contour plots of the resultant local velocity (u), along with the streamlines. The second row, (c) and (d), and the third row, (e) and (f), respectively, represent the corresponding distributions of the axial (u_x) and transverse (u_y) components of the local velocity.

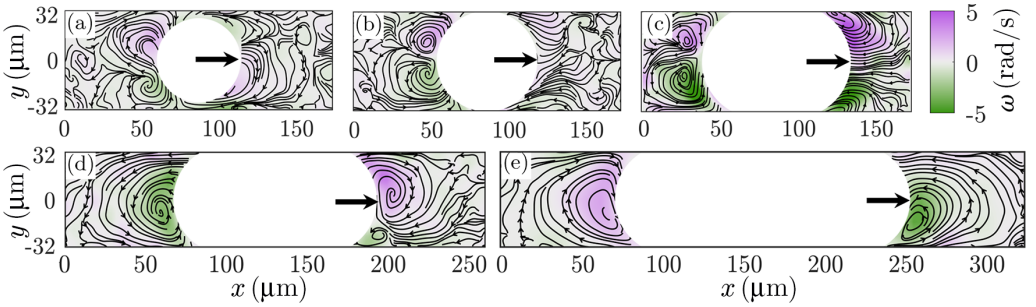

FIG. 4. Experimentally evaluated variations in the vorticity (ω) distribution for the active droplet velocity field with increasing effect of the confinement (κ). From panels (a) to (e), κ increases as $\kappa = 0.85$, $\kappa = 1.00$, $\kappa = 1.50$, $\kappa = 2.25$, and $\kappa = 3.00$.

band filter to visualize the trail of filled micelles containing the doped oil molecules which now fluoresce. During the image recording (at 25 fps), we adjust the exposure such that the filled micelle trail is clearly visible without over-saturating the pixels around the swimming droplet. We extract the fluorescence signal intensity (I) along the droplet interface precisely at a distance of 14 μm outside its circumference using a separate in-house Matlab code.

At each instant of time over a propulsion period of about 20 s, we extract the pixel intensity I along the droplet interface (always at a distance of about 14 μm outside the interface) by scanning following a clockwise rotation about the droplet centroid, starting from the x axis which is aligned with the channel center-line (Fig. 5). The angular (θ) position $[0, 2\pi]$ represents the anterior apex of the active droplet aligned with its swimming direction, while the angular position ($\theta = \pi$) represents the diametrically opposite posterior apex of the swimming droplet. We plot the temporal variation of I along the circumference from $[0, 2\pi]$ over a period of about 20 s to generate the kymographs shown in Fig. 5 (right column). Here, the intensity values are nondimensionalized by the maximum intensity value ($I_{\max}$) among all the experiments. We repeat identical experiments and post-processing methodology to generate the kymographs for droplets swimming with increasing values of κ.

III. NUMERICAL SIMULATION

A. Governing equations and boundary conditions

The physicochemical hydrodynamics of chemically active droplets is governed by the nonlinear coupling between fluid flow and chemical transport of surfactant monomer, filled/swollen micelles and empty micelles. We simplify the physical system by using a reference model [39,67,68] in which the chemical transport outside the droplet phase is modeled as a simple advection-diffusion process of surfactant molecules that is consumed at the droplet interface at a fixed rate. The velocity ($\boldsymbol{u}$) and pressure (p) fields are governed by the continuity and Navier-Stokes equations of the form [39]

$$\nabla \cdot \boldsymbol{u}_{i,e} = 0, \tag{1a}$$

$$\rho_{i,e}\left(\frac{\partial \boldsymbol{u}_{i,e}}{\partial t} + \boldsymbol{u}_{i,e} \cdot \nabla \boldsymbol{u}_{i,e}\right) = -\nabla p_{i,e} + \mu_{i,e} \nabla \boldsymbol{u}_{i,e}, \tag{1b}$$

where ρ is the density and μ is the dynamic viscosity. Subscripts i and e denote droplet phase and suspending phase, respectively. At the fluid-fluid interface, the interacting fluids satisfy velocity continuity and kinematic conditions

$$\boldsymbol{u}_i = \boldsymbol{u}_e, \tag{2a}$$

$$\frac{d\boldsymbol{x}_s}{dt} = (\boldsymbol{u}_e \cdot \boldsymbol{n})\boldsymbol{n}, \tag{2b}$$

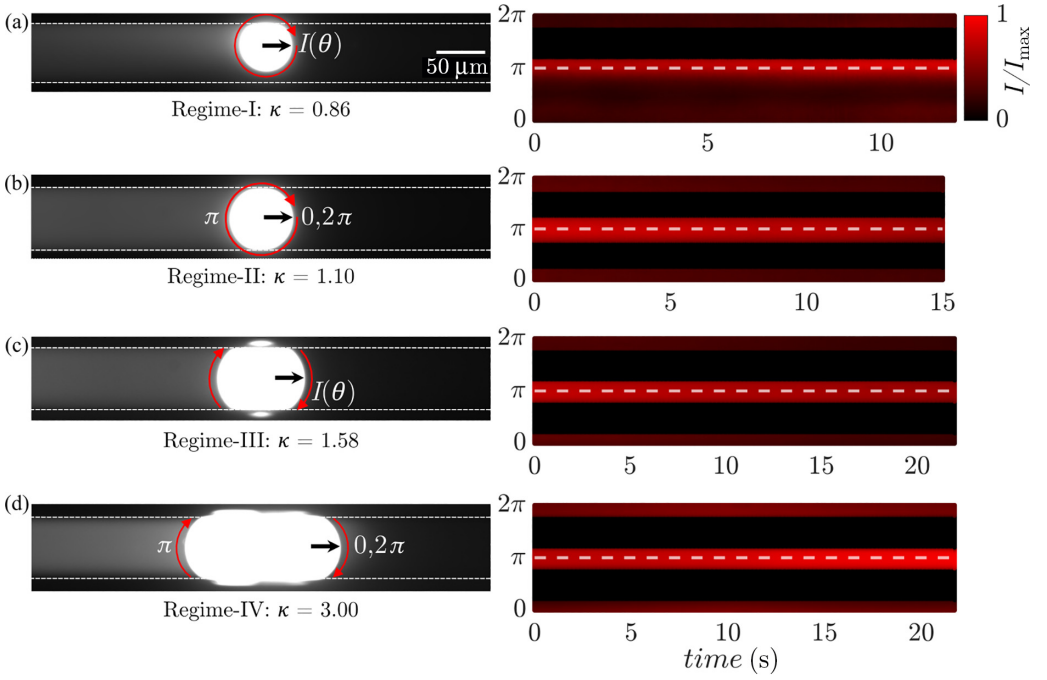

FIG. 5. Fluorescence microscopy images showing the filled micelle trail behind the active droplet (left column), and the corresponding kymographs (right column) representing the temporal evolution of the intensity profile $I(\theta)$ (filled micelle concentration) around the droplet interface over 20 s of propulsion. From top row to bottom row, results are presented for increasing effect of the confinement (κ) over the four regimes. For the kymographs, the fluorescence intensity (I) for the filled micelle is normalized by the maximum interfacial intensity ($I_{\max}$) for $\kappa = 3.00$.

where $\boldsymbol{x}_s$ represents the interface position and $\boldsymbol{n}$ represents the outward unit normal (directed away from the droplet phase). The stress balance at the fluid-fluid interface is given by [69]

$$\boldsymbol{n} \cdot (\boldsymbol{\sigma}_i - \boldsymbol{\sigma}_e) = \gamma(\nabla_s \cdot \boldsymbol{n})\boldsymbol{n} - \nabla_s \gamma, \tag{3}$$

where $\boldsymbol{\sigma}$ is stress tensor and γ is the surface tension. It is important to note that for chemically active droplets the fluid flow is coupled to the surfactant transport via the interfacial Marangoni stress (represented by the gradient of surface tension term in stress balance equation). The surface tension depends on the surfactant concentration as [69] $\gamma = \gamma_0 - \gamma_c(C - C_\infty + AR/D)$, where C is the surfactant concentration, C_∞ is the far-field surfactant concentration and R is the length scale. Here, γ_0 and γ_c are positive constants signifying reference surface tension at $C = C_\infty - AR/D$ and $\gamma_c \equiv (d\gamma/dC)|_{C=C_\infty - AR/D}$, respectively. The surfactant concentration outside the droplet is governed by an advection-diffusion equation of the form [39]

$$\frac{\partial C}{\partial t} + \boldsymbol{u}_e \cdot \nabla C = D\nabla^2 C, \tag{4}$$

where D is the molecular diffusivity of surfactant. As the droplet consumes surfactants at a constant rate, the diffusion flux at the droplet interface is given as

$$D\boldsymbol{n} \cdot \nabla C = A, \tag{5}$$

where A (> 0) is the constant rate of consumption. The bounding walls do not consume surfactants, thus the boundary condition at the walls are no-slip and no-penetration for velocity field, and

no-flux condition for surfactant concentration:

$$D\boldsymbol{n}_w \cdot \nabla C = 0, \tag{6}$$

where $\boldsymbol{n}_w$ represents the outward unit normal (directed away from the wall).

We have nondimensionalized the mathematical model using the following characteristic scales: confinement length scale R as the characteristic length scale, AR/D as the concentration scale, $\mathcal{U} = A\gamma_c R/[D(2\mu_e + 3\mu_i)]$ as the velocity scale, $R/\mathcal{U}$ as the timescale, and $\mu_e\mathcal{U}/R$ as the pressure scale. This nondimensionalization scheme yields the following dimensionless numbers: Reynolds number $\mathrm{Re} = \rho_e\mathcal{U}R/\mu_e$, capillary number $\mathrm{Ca} = \mu_e\mathcal{U}/\gamma_o$, Péclet number $\mathrm{Pe} = \mathcal{U}R/D$, confinement ratio $\kappa = D_d/2R$, density ratio ρ_i/ρ_e, and viscosity ratio μ_i/μ_e. The nondimensional variables obtained from the numerical simulation are represented with asterisk as superscript.

B. Solution methodology

To perform the numerical simulations, we have solved the governing differential equations for surfactant concentration, velocity and pressure fields along with boundary conditions [Eqs. (1)–(6)] using the finite-element solver COMSOL multiphysics. We have used the "laminar flow," "convection-diffusion equation," and "moving mesh" modules of COMSOL multiphysics to model the coupled nonlinear system. The "moving mesh" module employs the arbitrary Lagrangian-Eulerian (ALE) method [70–73] along with automatic remeshing algorithm to capture the transient dynamics of the moving and deforming fluid-fluid interface. All the simulations are performed in a two-dimensional cylindrical domain of radius R and length $30R$. To avoid large deformation of fluid-fluid interface, we solve the problem in a comoving reference frame in which reference frame translates with the droplet along the channel axis. In this comoving frame, the droplet velocity appears in the far-field and wall velocity condition. The droplet velocity is obtained by imposing an integral constraint following [72,73]. For spatial discretization, we use quadratic element for velocity and linear element for pressure and surfactant concentration. We use triangular mesh elements of very fine mesh refinement close to the droplet interface and the nearby boundary. For time discretization, we use second-order backward differentiation formula (BDF). In-built parallel direct sparse solver (PARDISO) is used to solve the discretized linear system with relative tolerance of 10^{-6}. We have validated our model with the existing literature (see Appendix A2, Fig. 9).

IV. RESULTS: EVOLUTION OF FLOW FIELD

In a quasi-2D reservoir, the active droplets of sizes comparable to those used in the experiments swim with a steady velocity, and by generating a dipolar velocity field (see Supplemental Material Fig. S2 [57]). In confinements, the swimming velocity of isotropic autophoretic spherical particles increases with increasing effect of confinement, as given by κ, reaching a peak value at a specific threshold ($\sim$0.7–0.8 for an isotropic spherical autophoretic particle in a capillary [56]). However, in narrow or tight confinements, such as in microchannels and microcapillaries with $\kappa > 0.7$–0.8, the swimming velocity of active droplets gradually decreases toward a constant value with increasing κ [55]. This is also observed for the experiments reported here [Fig. 1(d)]. The steady-state swimming speed (u_d) of the active droplet decreases with increasing κ, reaching a small average value of approximately 1 μm/s for $\kappa \sim 8$ [Fig. 1(d) and its inset]. Note that beyond $\kappa > 10$, the active droplet ceases to effectively squeeze through the microchannel (see Supplemental Material Fig. S6 [57]). In this regime, over which u_d decreases with increasing κ, hydrodynamics in the thin lubrication film between the active droplet and the walls of the microchannel plays a dominant role in dictating the swimming dynamics [55,56]. Here, we explain the evolution and characteristics of the hydrodynamic signature, or the flow field, generated by the active droplet as it swims in this same regime. To this end, we divide the swimming of the active droplet with varying κ into four regimes [Fig. 1(d)] based on the observed characteristics of the velocity field.

A. Regime-I: $0.70 < \kappa < 0.90$

In Regime-I, the spherical droplet microswimmer swims by generating a quadrupolar velocity field (Fig. 2(a); see Supplemental Video S1 [57]). Based on the higher local velocity ($\boldsymbol{u}$) in the posterior interfacial region between the microswimmer and the microchannel walls and the far-field hydrodynamic signature, the droplet microswimmer can be classified as a "pusher" in Regime-I. The velocity field is approximately symmetric about the x axis, with two circulation zones in each of the anterior and posterior regions of the droplet microswimmer [Fig. 2(a)]. The orientation of the vorticity (ω) associated with the two circulations zones [Fig. 4(a)], both at the anterior and posterior, are opposite to each other. Here, negative and positive values of ω represent anti-clockwise (orientation along the positive z axis) and clockwise (orientation along negative z axis) orientations of the vorticity, or angular velocity, of the flow field about the positive x axis. The distributions of the axial component (u_x) [Fig. 2(b)] and the transverse component (u_y) [Fig. 2(c)] of the local velocity are approximately symmetric and skew-symmetric about the x axis, respectively. u_x about the anterior apex is comparable to the steady swimming speed of the droplet microswimmer [Fig. 2(b)]. Note that the disturbance velocity decreases away from the droplet microswimmer as expected. In this regime, as the droplet microswimmer swims through the microchannel, it leaves behind a trail of filled micelles which tend to accumulate close to the posterior apex (i.e., about an orientation angle of π relative to the positive x axis), with a slight displacement toward the adjacent wall [kymograph in Fig. 5(a)]. The dark bands in the kymographs represent the microchannel walls.

B. Regime-II: $0.90 < \kappa < 1.30$

In Regime-II, for the tight fitting almost spherical droplet microswimmer, the flow velocity about the anterior apex is oriented toward the droplet instead of away from it as in Regime-I (compare Figs. 2(d) and 2(a); see Supplemental Video S2 [57]). Accordingly, ω associated with the two anterior circulation zones of the quadrupolar flow field has orientation opposite to that in Regime-I [compare Figs. 4(b) and 4(a)]. In this case, u is relatively higher in the anterior, instead of the posterior, interfacial region between the microswimmer and the walls of the microchannels [compare Figs. 2(d) and 2(a)]. The circulation zones at the posterior of the droplet microswimmer still persist [Fig. 4(b)] with ω comparable to that in Regime I.

In Regime-II, the distribution of u_x in the anterior region of the droplet microswimmer is apparently completely negative [Fig. 2(e)]. This seems contradictory to the fact that the droplet is still swimming along the positive x axis, as has been also noted previously [55]. However, using high-resolution μPIV analysis, we observe that u_x is actually positive near the anterior apex, with values comparable to the droplet swimming velocity (see Supplemental Material Fig. S3 [57]). This also implies that the stagnation point is imperceptibly close to the anterior apex of the droplet. The distribution of u_y remains skew-symmetric about the x axis, and comparable to that in Regime-I [compare Figs. 2(f) and 2(c)]. In Regime-II, the filled micelle trail spans uniformly over the entire width of the microchannel at the posterior end of the droplet microswimmer, instead of about the posterior apex as in Regime-I [kymograph in Fig. 5(b)].

C. Regime-III: $1.30 < \kappa < 1.80$

In Regime-III, the droplet microswimmer adapts to the tighter confinement by assuming a “stadiumlike” shape [64] [Fig. 2(g)]. It still swims by generating a quadrupolar velocity field with ω having the same orientation as in Regime-II, but having relatively higher magnitude (compare Figs. 4(c) and 4(b); see Supplemental Video S3 [57]). There are two differences between Regimes II and III—(i) the higher value of u is displaced more toward the anterior apex away from the interfacial region between the microchannel wall and the microswimmer as in Regime-II [compare Figs. 2(g) and 2(d)]; (ii) the distribution of u_x becomes increasingly negative in the anterior region of the droplet microswimmer [compare Figs. 2(h) and 2(e)]. In this case, we think that there is still an increasingly small region of positive u_x about the anterior apex of the droplet microswimmer, which

is difficult to resolve even with our high-resolution μPIV. The distribution of u_y [Fig. 2(i)], and the characteristics of the filled micelle tail at the posterior of the droplet microswimmer [kymograph in Fig. 5(c)] remain qualitatively similar to those in Regime-II.

D. Regime-IV: $\kappa > 1.80$

Finally, in Regime-IV, the droplet microswimmer swims in the tighter confinement by adopting an elongated "capsulelike" shape [65] (Figs. 3(a) and 3(b); See Supplemental Videos S4 and S5 [57]). Interestingly, in this regime the velocity field (flow pattern) becomes asymmetric about the x axis [Figs. 3(a) and 3(b)]. This asymmetric swimming regime has been partially observed before in microcapillaries [55]. Here we explain in detail the salient features of this unique regime.

The gradual evolution of the asymmetric flow pattern from the symmetric one, i.e., the emergence of Regime IV from Regime III, with increasing confinement effect is shown in Supplemental Material Fig. S4 [57]. The flow pattern in Regime IV is characterized by two dominant circulation zones, one each at the anterior and posterior of the droplet microswimmer [Figs. 3(a) and 3(b)]. The orientation of ω corresponding to these two circulation zones are always opposite to each other, i.e., if ω for the anterior zone is clockwise, then that for the posterior zone is always counterclockwise, and vice versa [compare Figs. 4(d) and 4(e)]. Note that with the variation in κ within Regime-IV, sometimes there is an emergence of a secondary weak circulation zone in the anterior of the droplet microswimmer [Figs. 3(a) and 4(d)]. This secondary circulation zone is unstable as its strength fluctuates with increasing κ within Regime-IV (Supplemental Material Fig. S5 [57]). But when this secondary circulation zone does exist, ω associated with it is always opposite to that of the dominant circulation zone at the anterior (Fig. 4(d) and Supplemental Material Figs. S5(b), S5(c), and S5(e) [57]).

In Regime-IV, on the one hand, the distribution of u_x becomes skew-symmetric, instead of symmetric, about the x axis [Figs. 3(c) and 3(d)], while on the other hand, the distribution of u_y loses its skew-symmetry about the x axis [Figs. 3(e) and 3(f)]. In this regime also, the filled micelle trail covers the entire width of the microchannel. But the concentration of the filled micelle at the posterior of the droplet microswimmer is higher compared to the other regimes [Fig. 5(d); compare the kymographs]. We also think that in this regime, there is nonzero concentration of filled micelles even in the anterior region of the microswimmer (compare the kymographs in Fig. 5).

The reduction in u_d with κ remains similar for increasing swimming medium viscosity (μ_e) compared to the constant active droplet viscosity (μ_i) as represented by the reducing value of the viscosity ratio $\lambda = \mu_i/\mu_e$ [Fig. 1(d)]. Furthermore, the shape adaptation of the active droplet, and the corresponding evolution in the velocity field, with increasing κ remain qualitatively similar for reducing values of λ (see Supplemental Material Sec. IV for details, and also see Supplemental Videos S6 [57]).

V. DISCUSSIONS

We explain the aforementioned evolution of the velocity field generated by the active droplet as it squeezes through increasingly tighter confinement (increasing κ) using the numerical simulation results shown in Figs. 6 and 7. The numerical simulation captures the gradual increase in the nondimensional swimming velocity (u_d^*) with increasing κ for weak confinements ($0.50 < \kappa < 0.70$) [Fig. 6(a)], as explained for isotropic autophoretic particles [56]. Importantly, the simulation also captures the gradual decrease in u_d^* with κ (> 0.70), as observed in the experiments [Fig. 1(d)].

In Regime-I ($\kappa \sim 0.85$), the nondimensional concentration of the surfactant monomer (C^*) reduces along the interface of the spherical active droplet, away from the anterior apex [Fig. 6(b)]. This is due to the spontaneous symmetry-breaking of the solute concentration under dominant advective effect, accentuated by the confinement [56]. Consequently, the interfacial surface tension (γ^*) gradually increases away from the anterior apex of the droplet microswimmer [Fig. 6(c)]. This results in the gradual increase of the Marangoni-stress driven interfacial velocity (u_s^*) [Fig. 6(b)],

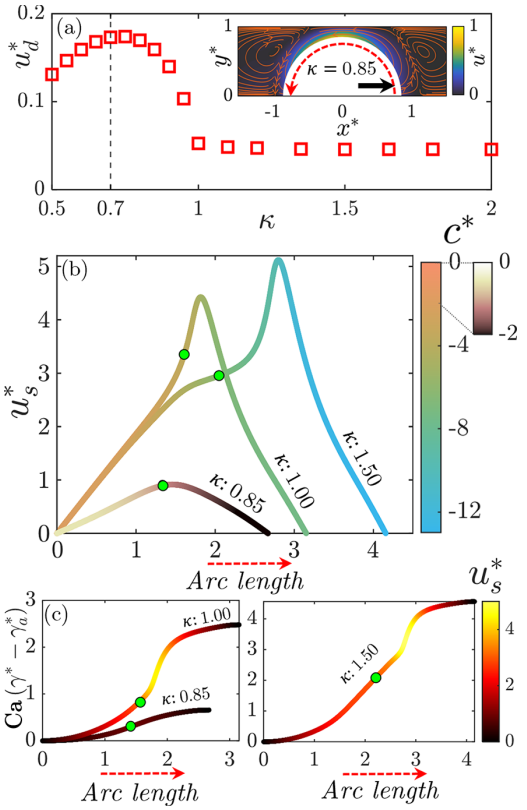

FIG. 6. Results from the numerical simulations. (a) Variation of the nondimensional droplet swimming velocity (u_d^*) with increasing confinement effect (κ). The inset shows the velocity contour plot along with the streamlines for the droplet microswimmer in Regime-I. (b) Variations of the nondimensional droplet interfacial velocity (u_s^*) with the arc length along the droplet interface for increasing values of κ over Regimes I–III. The arc length increases from the anterior apex (0) toward the posterior apex (dotted red arrow in inset in (a); also see Fig. 7). The graphs are color-coded with the nondimensional surfactant monomer concentration (C^*) along the interface. (c) Variations of the nondimensional interfacial tension (γ^*) for the active droplet for Regime-I: $\kappa = 0.85$, Regime-II: $\kappa = 1.00$ (left), and Regime-III: $\kappa = 1.50$ (right). γ^* is rescaled to the interfacial tension at the anterior apex (γ_a^*), and then multiplied by the constant capillary number (Ca).The graphs are color-coded with the corresponding magnitude of u_s^*. The green circles represent the location of the equator for spherical, or almost spherical, droplets, and the location of the middle transverse plane for the stadium-shaped droplet. We consider the following simulation parameters: $\mathrm{Re} = 10^{-3}$, $\mathrm{Ca} = 10^{-3}$, $\rho_i/\rho_e = 1$, $\mu_i/\mu_e = 138$, and $\mathrm{Pe} = 10$.

responsible for the self-propulsion of active droplets. Note that the peak value of u_s^* is reached in the posterior half of the droplet microswimmer, just beyond the equator [green circle in Fig. 6(b)]. This variation of u_s^* is commensurate with the quadrupolar velocity field, with liquid moving out of the anterior and posterior ends of the droplet microswimmer as observed in Regime-I [compare inset in Fig. 6(a) and Fig. 2(a); also compare streamlines in Figs. 7(a) and 2(a)].

In Regime-II ($\kappa \sim 1.00$), the gradient (decrease) in C^* along the droplet interface is relatively higher over the anterior half of the tight-fitting, almost spherical droplet microswimmer [Fig. 6(b)]. Consequently, there is steeper increases in γ^* over the anterior half [Fig. 6(c)]. This results in almost two-three times increase in u_s^* over the anterior half of the droplet microswimmer compared to Regime-I [Fig. 6(b)]. This enhanced u_s^* is instrumental in driving the liquid through the thin

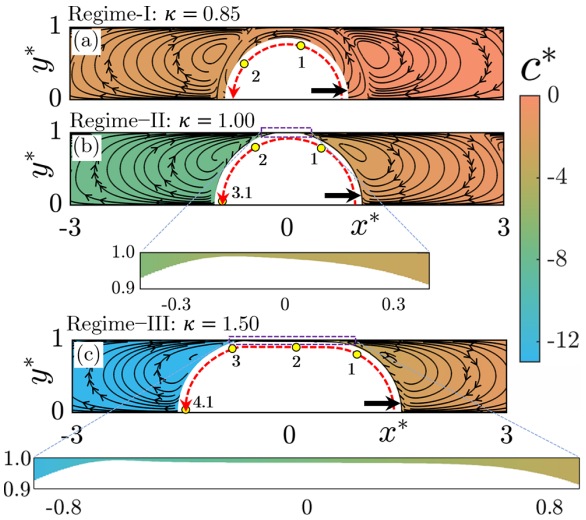

FIG. 7. Results from numerical simulation. (a), (b), and (c) represent the streamlines for the velocity field generated by the active droplet for Regime-I: $\kappa = 0.85$, Regime-II: $\kappa = 1.00$, and Regime-III: $\kappa = 1.50$, respectively. The streamlines are plotted on top of the corresponding contour plots for the nondimensional surfactant monomer concentration (C^*). For the axisymmetric simulations, only the top half has been shown here.

lubrication film which now exists between the droplet interface and the microchannel wall, about the droplet equator. For the droplet microswimmer to swim through the tight microchannel, it must transport the displaced liquid from the anterior to the posterior through the thin liquid film to satisfy continuity. This is facilitated by the higher value of u_s^*. The necessity of transporting the liquid from the anterior to the posterior through the thin film region changes the direction of the flow velocity in the anterior region toward the droplet microswimmer in Regime-II, as compared to away from it in Regime-I [compare streamlines in Figs. 7(b) and 2(d)]. The distributions of u_x, u_y, and ω follow consequently. Note that the flow field remains quadrupolar in nature in Regime-II.

The aforementioned increase in u_s^* does not translate to increased u_d^* in Regime-II. This can be understood as follows—a balance between the energies associated with the motion of the droplet microswimmer and the viscous dissipation in the thin film region shows that $u_d^* \sim u_s^*(1-\kappa)^{1/2}$. From Regime-I to Regime-II, $(1-\kappa)$ reduces from $\sim O(10^{-1})$ to at least $\sim O(10^{-3})$, assuming that the thickness of the intervening thin film in Regime-II is $\sim O(100)$ nm, if not smaller. Hence, u_d^* reduces since $(1-\kappa)$ reduces by two orders of magnitude, while u_s^* still remains $O(1)$ [Fig. 6(b)].

The peak in u_s^* beyond the equator observed in the numerical simulations [Fig. 6(b)] is due to a local sharp reduction in C^* [and hence, a sharp increase in γ^*; Fig. 6(c)] stemming from a local deformation in the droplet interface toward the posterior end of the thin film region [Fig. 7(b)]. We are unable to clearly discern such deformation in the experiments reported here. Beyond the location of this peak in u_s^*, the gradient in C^* becomes weak. C^* asymptotically approaches an almost constant value over the posterior droplet interface [Fig. 6(b)]. In the thin lubrication film between the droplet interface and the nonpenetrable, rigid wall, the concentration of surfactant monomers tends to rapidly homogenize due to the faster diffusion-driven transport in the thin region. Given that the surfactant consumption rate is also constant over the entire droplet interface, there is stronger depletion of C^* [Fig. 7(b)] over the thin film region [steeper increase in γ^*; Fig. 6(c)], especially toward its posterior end. Beyond this, once the thin region starts to widen, the concentration of surfactant monomers is already strongly depleted, and this results in a weak gradient in C^* over the posterior droplet interface. Consequently, γ^* becomes asymptotically constant over the posterior interface [Fig. 6(c)], beyond the peak in u_s^*, resulting in a sharp decrease in u_s^*. Hence, the flow field

at the posterior end, with two circulation zones, is not a Marangoni-stress dominated phenomenon, but also a consequence of the continuity of the flow between the thin film region and the posterior part of the droplet microswimmer. Overall, there appears to be a sharp fore-aft contrast in C^* over the droplet microswimmer length scale (i.e., D_d) in Regime-II [contour plot in Fig. 7(b)]. However, most of the reduction in C^* is actually in the anterior part of the microswimmer and over the thin film region, and not over the posterior part [Fig. 6(b)]. The sharp fore-aft contrast in the filled micelle concentration observed across the droplet microswimmer from the kymograph for Regime-II [Fig. 5(b)] is analogous to the aforementioned distribution of C^*. The kymograph also establishes the stability of the physicochemical mechanism underlying the droplet microswimmer propulsion in Regime-II.

In Regime-III ($\kappa \sim 1.50$), as the droplet microswimmer adapts to the tighter confinement by adopting a "stadiumlike" shape, the thin film region gets extended [Fig. 7(c)]. The elongated droplet microswimmer maintains a velocity field similar to that in Regime-II to transport liquid from the anterior to the posterior through the extended lubrication film [compare streamlines in Figs. 7(c) and 2(g)]. The shape of the droplet microswimmer necessitates the greater magnitude of ω for the anterior circulation zones. Over the ensuing thin film region, the gradient (decrease) of C^* along the droplet interface is almost linear culminating in a linear increase in γ^* [Fig. 6(c)]. This results in an almost uniform value of u_s^* over the thin film region in Regime-III due to the constant Marangoni stress [Fig. 6(b)]. Hence, although the variation in u_s^* over the anterior droplet interface remains similar in Regimes II and III, the gradient of u_s^* over the droplet interface in the thin film region becomes weaker in the latter [Fig. 6(b)]. Consequently, u_s^* attains a smaller value in the thin film region for Regime-III as compared to Regime-II. As a result, u_d^* is relatively smaller in Regime-III, albeit slightly, following the aforementioned scaling argument, and assuming that $(1 - \kappa)$ remains comparable in both the regimes. In Regime-III, there is more depletion of C^* over the longer thin film region resulting in greater fore-aft surfactant monomer contrast compared to Regime-II [compare Figs. 7(c) and 7(b)]. It is difficult to comment whether this translates to greater concentration of filled micelles at the posterior of the droplet microswimmer in Regime-III, since the fluorescence intensity from the kymographs looks comparable for Regimes II and III [compare Figs. 5(b) and 5(c)].

It is impossible to capture the asymmetric velocity field for the droplet microswimmer in Regime-IV using the present axisymmetric numerical simulation framework. Furthermore, a direct 3D numerical simulation of the capsule-shaped droplet microswimmer is beyond the scope of the present work. Based on our experimental observations, we speculate the following– as the active droplet becomes further elongated, the thin film region also gets elongated. The increasing Marangoni stress over the anterior cap of the droplet microswimmer triggers considerable liquid flux which needs to pass through the elongated thin film region with constant Marangoni stress, to satisfy continuity. The local pressure variation may result in asymmetric shape of the thin film, allowing for an asymmetric velocity field that satisfies the incompressible flow condition. The extended thin film region and the single circulation zone at the posterior are responsible for the enhanced accumulation of the filled micelles as seen from the kymograph [Fig. 5(d)]. Furthermore, the single circulation zone at the anterior may be responsible for a slight accumulation of filled micelles even at the front of the droplet microswimmer.

VI. CONCLUSIONS AND OUTLOOK

In this work, we try to provide a physical understanding of the alterations in the velocity field generated by active droplets as they adapt their shape and autonomously squeeze through increasingly tighter microconfinements. We do this by first analyzing the alterations in the velocity field using fluorescence microscopy and μ-PIV techniques. Then we try to correlate the observed flow fields to the underlying physicochemical hydrodynamics of active droplets in tight confinements, in the presence of a thin lubrication film. This is achieved using the results from finite-element based numerical simulations.

In a strong confinement (Regime-I), the active droplet swims with a quadrupolar flow field, by pushing liquid from the anterior and posterior ends. When the droplet microswimmer diameter becomes comparable to the microchannel length scale (Regime-II), for the still spherical droplet, the greater decrease in the surfactant monomer concentration over the anterior interface results in stronger Marangoni-stress driven interfacial velocity. This helps to transport the surrounding liquid from the anterior to the posterior of the droplet microswimmer through the thin film region which now exists between the microswimmer and the microchannel walls. We think that the geometry of the flow domain, along with the aforementioned constraint of transporting liquid through the thin film, changes the direction of the flow velocity in the anterior region toward the microswimmer, i.e., opposite to the swimming direction. The dissipation in the thin lubrication film dictates that the terminal velocity of the microswimmer reduces despite the increase in the interfacial velocity. Furthermore, the greater decrease in the surfactant monomer concentration over the anterior part of the droplet microswimmer, specifically in the thin film region, results in sharper fore-aft concentration gradient across the droplet microswimmer as compared to Regime-I. This is also evidenced from the filled micelle kymographs plotted for the active droplets.

When the microchannel length scale becomes smaller than the droplet microswimmer length scale, i.e., for confinement ratio greater than 1, the active droplet first adopts a "stadiumlike" shape as it squeezes through the tighter confinement (Regime-III). As the thin lubrication film gets extended because of this shape, the microswimmer maintains a quadrupolar flow field, with the velocity vectors oriented toward it in the anterior region, to squeeze through by transporting liquid through the thin film. Interestingly, the decrease in the interfacial surfactant concentration, and the corresponding variation in the interfacial tension, are almost linear in the extended thin film region. Consequently, the Marangoni stress-driven interfacial velocity is almost constant in the thin film region culminating in the slight decrease in the terminal velocity in Regime III as compared to Regime II. In Regime III, the greater decrease in the surfactant concentration over the extended lubrication film results in even sharper fore-aft gradient in the surfactant concentration across the droplet microswimmer as compared to Regime II. Unfortunately, this cannot be clearly inferred by comparing the kymographs for Regimes II and III.

As the confinement ratio further increases, the droplet microswimmer adopts an elongated, "capsulelike" shape (Regime-IV). As the droplet microswimmer gets elongated, we speculate that the local variation in Marangoni stress, and the constraints of the incompressible flow through the extended thin film region, result in an asymmetric shape of the thin film and an asymmetric velocity field. We further conclude that the single circulation zones observed in the anterior and posterior of the elongated droplet microswimmer are responsible for the enhanced concentration of filled micelles in the immediate vicinity of microswimmer, as observed in the corresponding kymographs. Finally, it should be noted that the the viscosity ratio between the active droplet and the swimming medium does not play a significant role in the aforementioned evolution of the velocity field with increasing confinement.

In future, it will be interesting to investigate the extent to which the evolution in the hydrodynamic signature demonstrated by active droplets in increasingly tighter confinements is comparable to the hydrodynamic adaptation of biological microswimmers under similar physical constraints. Such studies can tell us whether hydrodynamics plays a crucial role in the survival strategies of severely confined microswimmers by increasing their nutrient uptake. The present results also indicate that since the velocity field generated by the self-propelled microswimmers changes with increasing confinement, their mutual interactions are also bound to change with tighter confinements. Our work also provides an understanding of the chemohydrodynamic characteristics that can be present in possible state-of-the-art applications involving active droplets as autonomous probes or delivery agents in complex environment, like in extremely tight microfluidic networks or porous media, unreachable by passive carriers.

ACKNOWLEDGMENTS

S.G. and S.S.S. acknowledge the Prime Minister's Research Fellowship (PMRF), a scheme by the Govt. of India to improve the quality of research in various research institutions in the country. S.G. and S.S.S. thank Dr. Lakshmana Dora Chandrala for the discussions regarding the uncertainty calculations. S.G. and S.S.S. acknowledge the help from Mr. Aneesha Kajampady in carrying out the pressure-driven flow experiments in the microchannel. S.M. gratefully acknowledges support from DST-SERB Grant No. EEQ/2021/000561. S.M. thanks Indian Science Technology and Engineering Facilities Map (I-STEM), a Program supported by the Office of the Principal Scientific Adviser to the Govt. of India, for enabling access to the COMSOL Multiphysics 6.0 software used to carry out the numerical simulations. R.D. gratefully acknowledges support from Science and Engineering Research Board (SERB), Department of Science and Technology (DST), Government of India, through Grant No. SRG/2021/000892. R.D. also acknowledges support from IIT Hyderabad through seed Grant No. SG 93.

APPENDIX A: DETAILS OF THE μPIV ANALYSIS

The prominent sources of errors in the μPIV analysis arise from two important factors: the selection of the size and the properties of the tracer particles. The tracer particles are assumed to be neutrally buoyant and follow the flow streamlines when the difference between the fluid and tracer particle velocity is minimal. This can be achieved by reducing the size of the particles and reducing the difference in the density of the particles and the flow medium [74]. To characterize the behavior of the tracer particles in the flow medium, we determine the response time of the tracer particles toward a flow using Newton's second law as $t_0 = \rho_p d_p^2/18\mu_f$, where ρ_p is the density and d_p is the diameter of the tracer particles, μ_f is the dynamic viscosity of the fluid medium [74]. The ratio of the response time of the particles to the advection timescale of the flow l/u_0 is known as Stokes number, where l is the characteristic length scale which can be taken as d_p and u_0 is the flow velocity. The Stokes number should be less than 0.1 to maintain the errors due to tracers less than 1% [75]. The stokes number for the fluorescent particles of size 500 nm (480 ± 16 nm) and density of 1055 kg/m^3 is of the order 10^{-7}. The velocity lag between the flow medium (7.5% aqueous surfactant solution) and the tracer particles is calculated using Stokes drag law given as $d_p^2(\rho_p - \rho_f)g/18\mu$, where g is acceleration due to gravity and subscripts p and f are for particle and fluid properties [74]. The velocity lag for these tracer particles is of the order 10^{-2} μm/s. Hence, all the μPIV analysis has been carried out with these tracer particles to minimize the uncertainty due to the particle selection.

These fluorescent particles are excited with a high-pressure mercury lamp (Nikon, Model : LH-M100C-1,100W) through a dual-band filter with maximum excitation/emission wavelengths 487/562 and 523/630 (Chroma Technology, Model No. 59009-ET-FITC/CY3). These fluorescent particles are suspended in distilled water. We mix these suspended particles with 7.5% aqueous surfactant solution in 1 : 20 volume ratio and sonicate the solution for 10 minutes to ensure proper mixing, and there is no coagulation. We then add the active droplets (stored in 0.1% aqueous surfactant solution) to the sonicated 7.5% surfactant solution containing the tracer particles (with the same ratio of 1 : 2 as mentioned earlier) to visualize the disturbance field around the droplet swimmers after injecting in the microchannels.

The μPIV analysis is carried out using MATLAB-based software PIVlab. For the μPIV analysis using PIVlab, we use the discrete Fourier transform (DFT) method to calculate the crosscorrelation matrix, which has the flexibility to give multiple passes. For the first pass, we take the 64 × 64 pixels interrogation area with a step size of 32 × 32 pixels followed by a second pass of 32 × 32 pixels interrogation area with a step size of 16 × 16 pixels with Gaussian 2x3-point sub-pixel estimator along with extreme correlation robustness.

The accuracy of a digital PIV experiment is largely affected by errors in the measurement of the displacement, such as bias error (ϵ_{bias}), which accounts for the accuracy of the measurements, and random error (ϵ_{rms}) represents the precision in the measurements [76]. Due to the uncertainty in the

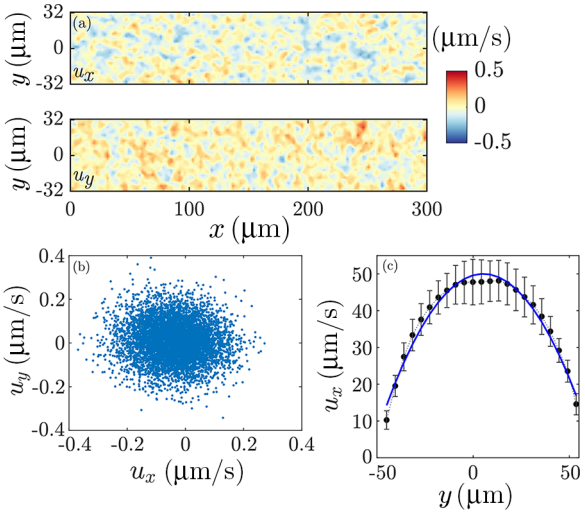

FIG. 8. μPIV analysis of quiescent medium seeded with 500 nm fluorescent particles exhibiting Brownian motion in a microchannel and with a prescribed pressure-driven flow. (a) The contour of u_x and u_y components of the particles within the microchannel. (b) Scatter plot of u_x vs u_y for the same. (c) Velocity measured using μPIV setup in a microchannel with the prescribed pressure-driven flow, a quadratic curve fitted to these data points along the channel width (solid blue line). x is along the length, and y is along the width of the microchannel as shown in Fig. 1(a).

displacement measurement, errors are bound to arise in the velocity measurements. The velocity due to the displacement of the particles can be written as $v = s\Delta X/\Delta t$, where s is the calibration factor, ΔX is the displacement of the particles in two consecutive frames, and Δt is the time step in such consecutive frames. The uncertainty in the velocity measurement is calculated using $U_v = [(\frac{\Delta X}{\Delta t}U_s)^2 + (\frac{s}{\Delta t}U_{\Delta X})^2 + (\frac{s\Delta X}{\Delta t^2}U_{\Delta t})^2]^{1/2}$ [77], where U_s is the uncertainty in calibration factor, $U_{\Delta X}$ is the total uncertainty in displacement measurement and $U_{\Delta t}$ is the uncertainty in time. In the present study, the time Δt between two consecutive frames is 0.04 s, and the uncertainty in time $U_{\Delta t}$ is 2×10^{-6} s. The calibration factor s for a 30× objective is 0.1762 μm/pixel, and the uncertainty in the measurement of the calibration factor U_s is 0.001379 μm/pixel. The maximum displacement ΔX for a velocity of 40 μm/s (Fig. 2) is taken as 9 pixels. The uncertainty in displacement measurement $U_{\Delta X} = (\epsilon_{\text{bias}}^2 + \epsilon_{\text{rms}}^2)^{1/2}$ for a particle image of 3×3 pixels (with a 30× objective to resolve 500 nm particle diameter) using a DFT multipass algorithm is taken as 0.02 pixel from [78]. Using the above equation, the uncertainty in the velocity measurement is found to be ±0.3225 μm/s, which is ±0.8 % of the maximum velocity.

We verify the results (flow field around the swimmer) obtained from the μPIV analysis are from the disturbance field generated due to the droplet self-propulsion and are not any noise coming from the analysis. To quantify the noise from the external medium in terms of velocity, experiments were carried out in a microchannel with a quiescent medium seeded with 500 nm fluorescent particles exhibiting Brownian motion. The net displacement of the particles undergoing Brownian motion is close to zero over time, so we have calculated the velocities over a time span of 19 s. The contour of the averaged x (u_x) and y (u_y) components of velocity for Brownian motion as shown in [Fig. 8(a)]. The minimum/maximum values of u_x and u_y components of velocity that we can detect for a particle undergoing Brownian motion in a quiescent medium is $-0.3690/0.2720$ μm/s and $-0.3422/0.3903$ μm/s [see Fig. 8(b)]. However, the average disturbance field velocity around the droplet for $\kappa = 0.85$ [Fig. 2(a)] at a distance $\sim R_d$ from its circumference is 7.169 ± 0.3312 μm/s. The velocity due to Brownian motion is very small compared to the magnitude of the disturbance field around the droplet, which implies that the velocity signal at a distance $\sim R_d$ from the

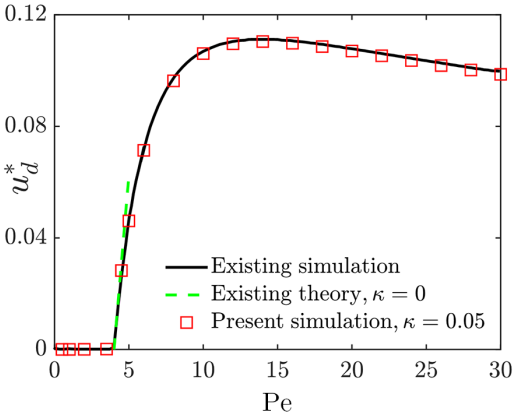

FIG. 9. Variation of steady swimming speed with Péclet number. The existing simulation data is taken from the supplementary material of [34] and the theoretical expression is reported in Ref. [68]. We consider the following simulation parameters: $\mathrm{Re} = 10^{-3}$, $\mathrm{Ca} = 10^{-3}$, $\rho_i/\rho_e = 1$, $\mu_i/\mu_e = 1/36$, and $\kappa = 0.05$. For this validation purpose, the droplet radius has been taken as the length scale.

circumference of the droplet is purely due to advection (self-propulsion) and not due to diffusive motion of the tracer particles.

We have also compared the velocity of a pressure-driven flow in the center plane calculated using the same μPIV setup in the x-direction (along the length) in a microchannel of the cross-sectional area of 100×50 μm^2 to a second-order polynomial, approximating a Hagen-Poiseuille flow in a channel as shown in Fig. 8(c). The μPIV velocity matches well with the second-order polynomial with an average standard deviation of ± 4.59704565 μm/s, indicating the PIV setup is robust enough to capture the accurate displacements of the tracer particles in the flow.

APPENDIX B: VALIDATION OF NUMERICAL METHOD

To assess the correctness of the present simulation method, we validate simulation results with existing literature. Figure 9 shows the variation of steady swimming speed of unconfined droplet as a function of Péclet number. In the absence of bounding walls (i.e., $\kappa = 0$), an active droplet remains motionless until $\mathrm{Pe} = 4$. At $\mathrm{Pe} = 4$ advection of surfactant transport is strong enough to make the motionless state unstable and the droplet starts to swim at a speed $(\mathrm{Pe} - 4)/16$ near $\mathrm{Pe} = 4$ [34,68]. Figure 9 shows that present simulation results compare well with the existing analytical and numerical results. To reduce the effect of bounding wall, we have chosen $\kappa = 0.05$.

[1] K. Tsuji, M. Asakawa, Y. Anzai, T. Sumino, and K. ichi Harada, Degradation of microcystins using immobilized microorganism isolated in an eutrophic lake, Chemosphere **65**, 117 (2006).

[2] M. Yamaguchi, Y. Mori, Y. Kozuka, H. Okada, K. Uematsu, A. Tame, H. Furukawa, T. Maruyama, C. O. Worman, and K. Yokoyama, Prokaryote or eukaryote? A unique microorganism from the deep sea, J. Electron Microsc. **61**, 423 (2012).

[3] L. Ranjard and A. Richaume, Quantitative and qualitative microscale distribution of bacteria in soil, Res. Microbiol. **152**, 707 (2001).

[4] D. Or, B. Smets, J. Wraith, A. Dechesne, and S. Friedman, Physical constraints affecting bacterial habitats and activity in unsaturated porous media—A review, Adv. Water Resour. **30**, 1505 (2007).

[5] S. Altveş, H. K. Yildiz, and H. C. Vural, Interaction of the microbiota with the human body in health and diseases, Biosci. Microbiota Food Health **39**, 23 (2020).

[6] E. Dekaboruah, M. V. Suryavanshi, D. Chettri, and A. K. Verma, Human microbiome: An academic update on human body site specific surveillance and its possible role, Arch. Microbiol. **202**, 2147 (2020).
[7] J. K. Carson, V. Gonzalez-Quiñones, D. V. Murphy, C. Hinz, J. A. Shaw, and D. B. Gleeson, Low pore connectivity increases bacterial diversity in soil, Appl. Environ. Microbiol. **76**, 3936 (2010).
[8] M. E. V. Johansson, J. K. Gustafsson, J. Holmén-Larsson, K. S. Jabbar, L. Xia, H. Xu, F. K. Ghishan, F. A. Carvalho, A. T. Gewirtz, H. Sjövall, and G. C. Hansson, Bacteria penetrate the normally impenetrable inner colon mucus layer in both murine colitis models and patients with ulcerative colitis, Gut **63**, 281 (2014).
[9] P. S. Cohen and D. C. Laux, [24] bacterial adhesion to and penetration of intestinal mucus *in vitro*, *Adhesion of Microbial Pathogens*, Methods in Enzymology, Vol. 253 (Academic Press, San Diego, CA, 1995), pp. 309–314.
[10] M. E. V. Johansson, J. K. Gustafsson, K. E. Sjöberg, J. Petersson, L. Holm, H. Sjövall, and G. C. Hansson, Bacteria penetrate the inner mucus layer before inflammation in the dextran sulfate colitis model, PLoS ONE **5**, e12238 (2010).
[11] G. Vizsnyiczai, G. Frangipane, S. Bianchi, F. Saglimbeni, D. Dell'Arciprete, and R. Leonardo, A transition to stable one-dimensional swimming enhances *E. coli* motility through narrow channels, Nat. Commun. **11**, 2340 (2020).
[12] V. Tokárová Jr, A. Sudalaiyadum Perumal, M. Nayak, H. Shum, O. Kaspar, K. Rajendran, M. Mohammadi, C. Tremblay, E. Gaffney, S. Martel, and D. Nicolau, Patterns of bacterial motility in microfluidics-confining environments, Proc. Natl. Acad. Sci. USA **118**, e2013925118 (2021).
[13] J. Männik, R. Driessen, P. Galajda, J. E. Keymer, and C. Dekker, Bacterial growth and motility in sub-micron constrictions, Proc. Natl. Acad. Sci. USA **106**, 14861 (2009).
[14] G. Noselli, A. Beran, M. Arroyo, and A. Desimone, Swimming euglena respond to confinement with a behavioral change enabling effective crawling, Nat. Phys. **15**, 496 (2019).
[15] S. Jana, S. H. Um, and S. Jung, Paramecium swimming in capillary tube, Phys. Fluids **24**, 041901 (2012).
[16] S. Jana, A. Eddins, C. Spoon, and S. Jung, Somersault of paramecium in extremely confined environments, Sci. Rep. **5**, 13148 (2015).
[17] M. Medina-Sánchez, H. Xu, and O. G. Schmidt, Micro- and nano-motors: The new generation of drug carriers, Ther. Deliv. **9**, 303 (2018).
[18] R. Lin, W. Yu, X. Chen, and H. Gao, Self-propelled micro/nanomotors for tumor targeting delivery and therapy, Adv. Healthcare Mater. **10**, 2001212 (2021).
[19] W. F. Paxton, K. C. Kistler, C. C. Olmeda, A. Sen, S. K. St. Angelo, Y. Cao, T. E. Mallouk, P. E. Lammert, and V. H. Crespi, Catalytic nanomotors: Autonomous movement of striped nanorods, J. Am. Chem. Soc. **126**, 13424 (2004).
[20] J. R. Howse, R. A. L. Jones, A. J. Ryan, T. Gough, R. Vafabakhsh, and R. Golestanian, Self-motile colloidal particles: From directed propulsion to random walk, Phys. Rev. Lett. **99**, 048102 (2007).
[21] A. Zöttl and H. Stark, Emergent behavior in active colloids, J. Phys.: Condens. Matter **28**, 253001 (2016).
[22] B. Liebchen and A. K. Mukhopadhyay, Interactions in active colloids, J. Phys.: Condens. Matter **34**, 083002 (2022).
[23] A. Zöttl and H. Stark, Modeling active colloids: From active Brownian particles to hydrodynamic and chemical fields, Annu. Rev. Condens. Matter Phys. **14**, 109 (2023).
[24] J. L. Anderson, Colloid transport by interfacial forces, Annu. Rev. Fluid Mech. **21**, 61 (1989).
[25] J. L. Moran and J. D. Posner, Phoretic self-propulsion, Annu. Rev. Fluid Mech. **49**, 511 (2017).
[26] R. Golestanian, T. B. Liverpool, and A. Ajdari, Propulsion of a molecular machine by asymmetric distribution of reaction products, Phys. Rev. Lett. **94**, 220801 (2005).
[27] M. Pumera, Electrochemically powered self-propelled electrophoretic nanosubmarines, Nanoscale **2**, 1643 (2010).
[28] H.-R. Jiang, N. Yoshinaga, and M. Sano, Active motion of a Janus particle by self-thermophoresis in a defocused laser beam, Phys. Rev. Lett. **105**, 268302 (2010).
[29] N. Yu, X. Lou, K. Chen, and M. Yang, Phototaxis of active colloids by self-thermophoresis, Soft Matter **15**, 408 (2019).

[30] T. Toyota, N. Maru, M. M. Hanczyc, T. Ikegami, and T. Sugawara, Self-propelled oil droplets consuming "fuel" surfactant, J. Am. Chem. Soc. **131**, 5012 (2009).
[31] S. Thutupalli, R. Seemann, and S. Herminghaus, Swarming behavior of simple model squirmers, New J. Phys. **13**, 073021 (2011).
[32] K. Peddireddy, P. Kumar, S. Thutupalli, S. Herminghaus, and C. Bahr, Solubilization of thermotropic liquid crystal compounds in aqueous surfactant solutions, Langmuir **28**, 12426 (2012).
[33] S. Herminghaus, C. C. Maass, C. Krüger, S. Thutupalli, L. Goehring, and C. Bahr, Interfacial mechanisms in active emulsions, Soft Matter **10**, 7008 (2014).
[34] Z. Izri, M. N. Van Der Linden, S. Michelin, and O. Dauchot, Self-propulsion of pure water droplets by spontaneous Marangoni-stress-driven motion, Phys. Rev. Lett. **113**, 248302 (2014).
[35] M. Suga, S. Suda, M. Ichikawa, and Y. Kimura, Self-propelled motion switching in nematic liquid crystal droplets in aqueous surfactant solutions, Phys. Rev. E **97**, 062703 (2018).
[36] C. C. Maass, C. Krüger, S. Herminghaus, and C. Bahr, Swimming droplets, Annu. Rev. Condens. Matter Phys. **7**, 171 (2016).
[37] S. Birrer, S. I. Cheon, and L. D. Zarzar, We the droplets: A constitutional approach to active and self-propelled emulsions, Curr. Opin. Colloid Interface Sci. **61**, 101623 (2022).
[38] P. Dwivedi, D. Pillai, and R. Mangal, Self-propelled swimming droplets, Curr. Opin. Colloid Interface Sci. **61**, 101614 (2022).
[39] S. Michelin, Self-propulsion of chemically active droplets, Annu. Rev. Fluid Mech. **55**, 77 (2023).
[40] Z. Xiao, M. Wei, and W. Wang, A review of micromotors in confinements: Pores, channels, grooves, steps, interfaces, chains, and swimming in the bulk, ACS Appl. Mater. Interfaces **11**, 6667 (2019).
[41] L. Zhu, E. Lauga, and L. Brandt, Low-Reynolds-number swimming in a capillary tube, J. Fluid Mech. **726**, 285 (2013).
[42] J. Elgeti and G. Gompper, Run-and-tumble dynamics of self-propelled particles in confinement, Europhys. Lett. **109**, 58003 (2015).
[43] J. de Graaf, A. J. T. M. Mathijssen, M. Fabritius, H. Menke, C. Holm, and T. N. Shendruk, Understanding the onset of oscillatory swimming in microchannels, Soft Matter **12**, 4704 (2016).
[44] O. Liot, M. Socol, L. Garcia, J. Thiéry, A. Figarol, A. F. Mingotaud, and P. Joseph, Transport of nano-objects in narrow channels: Influence of Brownian diffusion, confinement and particle nature, J. Phys.: Condens. Matter **30**, 234001 (2018).
[45] P. Ahana and S. P. Thampi, Confinement induced trajectory of a squirmer in a two dimensional channel, Fluid Dyn. Res. **51**, 065504 (2019).
[46] A. Dhar, P. S. Burada, and G. P. R. Sekhar, Hydrodynamics of active particles confined in a periodically tapered channel, Phys. Fluids **32**, 102005 (2020).
[47] J. Simmchen, J. Katuri, W. E. Uspal, M. N. Popescu, M. Tasinkevych, and S. Sánchez, Topographical pathways guide chemical microswimmers, Nat. Commun. **7**, 10598 (2016).
[48] C. Liu, C. Zhou, W. Wang, and H. P. Zhang, Bimetallic microswimmers speed up in confining channels, Phys. Rev. Lett. **117**, 198001 (2016).
[49] C. de Blois, M. Reyssat, S. Michelin, and O. Dauchot, Flow field around a confined active droplet, Phys. Rev. Fluids **4**, 054001 (2019).
[50] C. Jin, C. Krüger, and C. C. Maass, Chemotaxis and autochemotaxis of self-propelling droplet swimmers, Proc. Natl. Acad. Sci. USA **114**, 5089 (2017).
[51] C. Jin, B. V. Hokmabad, K. A. Baldwin, and C. C. Maass, Chemotactic droplet swimmers in complex geometries, J. Phys.: Condens. Matter **30**, 054003 (2018).
[52] C. Jin, J. Vachier, S. Bandyopadhyay, T. Macharashvili, and C. C. Maass, Fine balance of chemotactic and hydrodynamic torques: When microswimmers orbit a pillar just once, Phys. Rev. E **100**, 040601(R) (2019).
[53] P. Ramesh, B. V. Hokmabad, D. O. Pushkin, A. J. Mathijssen, and C. C. Maass, Interfacial activity dynamics of confined active droplets, J. Fluid Mech. **966**, A29 (2023).
[54] P. Kumar, P. Dwivedi, S. Ashraf, D. Pillai, and R. Mangal, Motility and pairwise interactions of chemically active droplets in one-dimensional confinement, Phys. Rev. E **110**, 024612 (2024).

[55] C. de Blois, V. Bertin, S. Suda, M. Ichikawa, M. Reyssat, and O. Dauchot, Swimming droplets in 1D geometries: An active Bretherton problem, Soft Matter **17**, 6646 (2021).
[56] F. Picella and S. Michelin, Confined self-propulsion of an isotropic active colloid, J. Fluid Mech. **933**, A27 (2022).
[57] See Supplemental Material at http://link.aps.org/supplemental/10.1103/PhysRevFluids.10.044202 for active droplet generation methodology, droplet's centroid tracking procedure, useful supplemental images, description of swimming in higher viscous medium and the supplemental videos, which includes Refs. [58–62].
[58] H. Nganguia and O. S. Pak, Squirming motion in a brinkman medium, J. Fluid Mech. **855**, 554 (2018).
[59] C. A. Schneider, W. S. Rasband, and K. W. Eliceiri, Nih image to imagej: 25 years of image analysis, Nat. Methods **9**, 671 (2012).
[60] W. Gilpin, V. N. Prakash, and M. Prakash, Flowtrace: Simple visualization of coherent structures in biological fluid flows, J. Exp. Biol. **220**, 3411 (2017).
[61] W. Gilpin, V. N. Prakash, and M. Prakash, Vortex arrays and ciliary tangles underlie the feeding-swimming trade-off in starfish larvae, Nat. Phys. **13**, 380 (2017).
[62] B. V. Hokmabad, R. Dey, M. Jalaal, D. Mohanty, M. Almukambetova, K. A. Baldwin, D. Lohse, and C. C. Maass, Emergence of bimodal motility in active droplets, Phys. Rev. X **11**, 011043 (2021).
[63] B. V. Hokmabad, J. Agudo-Canalejo, S. Saha, R. Golestanian, and C. C. Maass, Chemotactic self-caging in active emulsions, Proc. Natl. Acad. Sci. USA **119**, e2122269119 (2022).
[64] E. W. Weisstein, Stadium, From *MathWorld*–A Wolfram Web Resource, https://mathworld.wolfram.com/Stadium.html.
[65] E. W. Weisstein, Capsule, From *MathWorld*–A Wolfram Web Resource, https://mathworld.wolfram.com/Capsule.html.
[66] W. Thielicke and E. Stamhuis, Pivlab–towards user-friendly, affordable and accurate digital particle image velocimetry in matlab, J. Open Res. Soft. **2**, 30 (2014).
[67] S. Michelin, E. Lauga, and D. Bartolo, Spontaneous autophoretic motion of isotropic particles, Phys. Fluids **25**, 061701 (2013).
[68] M. Morozov and S. Michelin, Nonlinear dynamics of a chemically-active drop: From steady to chaotic self-propulsion, J. Chem. Phys. **150**, 044110 (2019).
[69] M. Morozov and S. Michelin, Self-propulsion near the onset of marangoni instability of deformable active droplets, J. Fluid Mech. **860**, 711 (2019).
[70] P. Hadikhani, S. M. H. Hashemi, G. Balestra, L. Zhu, M. A. Modestino, F. Gallaire, and D. Psaltis, Inertial manipulation of bubbles in rectangular microfluidic channels, Lab Chip **18**, 1035 (2018).
[71] Y. E. Yu, L. Zhu, S. Shim, J. Eggers, and H. A. Stone, Time-dependent motion of a confined bubble in a tube: Transition between two steady states, J. Fluid Mech. **857**, R4 (2018).
[72] G. Balestra, L. Zhu, and F. Gallaire, Viscous taylor droplets in axisymmetric and planar tubes: From Bretherton's theory to empirical models, Microfluid. Nanofluid. **22**, 67 (2018).
[73] Q. Mao, Q.-J. Yang, D.-X. Wang, and W. Cao, Effect of soluble surfactant on the interface dynamics of a rising droplet, Phys. Fluids **35**, 062112 (2023).
[74] M. Raffel, C. E. Willert, F. Scarano, C. J. Kähler, S. T. Wereley, and J. Kompenhans, *Particle Image Velocimetry: A Practical Guide* (Springer, Berlin, 2018).
[75] C. Tropea, A. Yarin, and J. Foss, *Springer Handbook of Experimental Fluid Mechanics*, Vol. 1 (Springer, Berlin, 2007).
[76] L. Gui and S. Wereley, A correlation-based continuous window-shift technique to reduce the peak-locking effect in digital piv image evaluation, Exp. Fluids **32**, 506 (2002).
[77] L. Chandrala, Unsteady evolution of compressible vortex rings: Velocity, density, and acoustic fields, Ph.D. thesis, Indian Institute of Technology Kanpur, Kanpur, India, 2016.
[78] W. Thielicke, The flapping flight of birds: Analysis and application, Ph.D. thesis, University of Groningen, The Netherlands, 2014.